PAPER

Microstructure evolution of sandwich graphite oxide/interlayer-embedded Au nanoparticles induced from *γ*-rays for carcinoembryonic antigen biosensor

IOP Publishing Nanotechnology
Nanotechnology 30 (2019) 495501 (12pp) https://doi.org/10.1088/1361-6528/ab3e1e

Microstructure evolution of sandwich graphite oxide/interlayer-embedded Au nanoparticles induced from γ-rays for carcinoembryonic antigen biosensor

Xiaomeng Zhao, Wei Wang, Liangsen Liu[1], Yanli Hu, Zhiwei Xu[1], Liyan Liu, Ning Wu and Nan Li

State Key Laboratory of Separation Membranes and Membrane Processes, School of Textile Science and Engineering, Tianjin Polytechnic University, Tianjin 300387, People's Republic of China

E-mail: 83019163@163.com and xuzhiwei@tjpu.edu.cn

Received 4 January 2019, revised 15 July 2019
Accepted for publication 23 August 2019
Published 23 September 2019

Abstract

With the capability of inducing small particle sizes of supported metal in graphite oxide (GO), the γ-ray irradiation method applied for preparing graphite oxide-gold (GO-Au) nanocomposites as electrochemical immunosensors has attracted specific attention recently. To study the accurate factors influencing the precise morphology and final performance of the prepared composites in the γ-irradiation system, we proposed a facile method to investigate the evolution of the GO structure, size and dispersion of Au nanoparticles (AuNPs) produced with the addition of isopropyl alcohol to the system. The GO-Au nanocomposites were characterized by Fourier transform infrared spectroscopy, x-ray diffraction spectra, Raman spectra, x-ray photoelectron spectroscopy and high resolution transmission electron microscopy. These nanocomposites with sandwich morphology exhibited an excellent immunosensor performance with a low detection limit of 15.8 pg ml^{-1} (S/N = 3) and a wide linear range from 1 to 40 ng ml^{-1} for detecting carcinoembryonic antigens. The enhanced biosensing performance is attributed to the synergistic effect of γ-irradiation and the precise structure of GO, which endows the smaller size and more uniform distribution of AuNPs on the GO as well as the good signal amplification capability. Furthermore, adopting the γ-irradiation method and use of GO as a precursor is propitious for application in large-scale production because of its high-efficiency and high-yielding characteristics.

Keywords: gamma irradiation, graphite oxide, gold nanoparticles, carcinoembryonic antigen detection

(Some figures may appear in colour only in the online journal)

1. Introduction

Currently, as one of the leading causes of death worldwide, cancer has caused great panic in the public calling for the characterization of the uncontrollable diffusion and growth of abnormal cells [1]. At present, there is no effective treatment for advanced cancer in the medical field, while early patients with few cancer cells in the body are still expected to be cured by timely and active treatment. Therefore, in order to reduce the incidence and mortality of cancer, accurate and effective early detection become essential to the medical field. Carcinoembryonic antigens (CEAs) are a kind of protein which extensively exists in the serum of cancer patients while just a low concentration can cause the immune response of patients.

[1] Authors to whom any correspondence should be addressed.

Hence, it is of great significance to monitor the level of CEA in serum which can also be used as a biomarker to determine if a person has cancer [2–4].

So far, CEA detection methods include radioimmunoassay, enzyme-linked immunoassay, time-resolved fluorescence, chemiluminescence, flow injection system based immunosensors, etc [5–9]. However, these methods have their own limits in preparation such as being unfriendly to the environment, time-consuming, difficult to achieve automation, or have poor accuracy [3, 5]. Recently, as an increasingly important means of clinical diagnosis in the field of immunochemistry that combines immunological technology with electrochemical analysis methods, electrochemical immunosensors have attracted much attention in the scientific community due to their range of advantages such as low detection limit, small amount of analytes demanded, simple instruments needed, convenient operation and so on [10, 11].

One of the most significant steps in building an electrochemical immunosensor is to effectively immobilize the biological recognition molecules on the detection interface [11–15]. As a two-dimensional carbon material, graphene has a series of unique physicochemical characteristics such as good conductivity, high specific surface area and biocompatibility which renders it an ideal functional material in many fields including combination with metals as an electrochemical sensing platform with enhanced electronic and catalytic properties [15–21]. With good electrical conductivity, large specific surface area, abundant surface active sites, strong adsorptive power and excellent biocompatibility [22–26], Au nanoparticles (AuNPs) can form strong bonds with positively charged groups of proteins or other biological macromolecules via electrostatic adsorption but does not cause denaturation to them after adsorption, which can then also be immobilized on electrodes by covalent bonding and electrostatic adsorption. Thus AuNPs have been commonly used as an efficient nanomaterial for the immobilization of biomolecules and markers for detecting antigens or antibodies in immunoreaction [27, 28]. Herein, graphene-gold nanocomposites have always been used for immunosensing experiments to date. So far, many methods have been used to prepare graphene-rare precious metal composites such as thermal treatment, laser ablation, dry plasma synthesis and chemical reduction [29–31], etc. Among all these methods, the radiation method is regarded as the most efficient and environmentally friendly as it does not demand extremely high temperatures or any chemical reducing agents [19, 32–37]. Nevertheless, few defects and a highly conjugated structure in the surface of graphene renders it difficult to react with other materials, thus scientists often use graphene oxide as the carrier to increase its reactive sites and the ability of supporting metal particles [38]. Whereas the prepared graphene oxide-Au composites often suffer from the problems of large particle size and uneven distribution of the supporting metal particles in the surface of graphene oxide, which may affect the further improvement of the immune performance of the prepared electrochemical immunosensors [39].

In our previous work, we demonstrated that graphite oxide (GO) has an interlamellar limit effect on the supporting silver nanoparticles which endows the small size of silver nanoparticles using a γ-irradiation process [16], thus in this work, we adopted GO directly as the carrier of the metals and hoped to obtain supporting AuNPs with small size in the prepared composites. While the accurate factors influencing the precise mophologies and final performance of the prepared composites still remained elusive in the γ-irradiation system, and herein we proposed a facile method to study the evolution of graphization and oxygen-containing groups on the graphene sheet and Au nanoparticle size and dispersion of the outcome with the addition of isopropyl alcohol (IPA) to the system. To the best of our knowledge, the project has not been researched in previous work. In this work, we designed a simple approach to prepare GO-Au nanocomposites as electrochemical immunosensors specific to CEA after being modified with anti-CEA by γ-irradiation assisted with a varying additive amount of IPA. The sandwich morphology of GO-Au nanoparticle composites was formed because Au ions are interlayer-embedded in GO and then *in situ* reduced by γ-irradiation. Various additive amounts of IPA endow the prepared GO-Au nanocomposites with different containing-oxygen groups and defects in GO, which in turn influences the final performance of the GO-Au nanocomposites as biosensors. Then we studied the structure of these prepared samples with Fourier transform infrared spectroscopy (FTIR), x-ray diffraction spectra (XRD), Raman spectra, x-ray photoelectron spectroscopy (XPS), high resolution transmission electron microscopy (HRTEM) and determined the performance of the samples with cyclic voltammograms (CV) and square wave voltammetry (SWV). The enhanced immunosensing performance of the prepared composites is attributed to the collaborative advantage of γ-irradiation and the interlamellar limit effect of GO, which endows a small size and uniform distribution of AuNPs in GO as well as good signal amplification capability.

2. Experimental

2.1. Chemicals and materials

Natural graphite flakes (200 mesh) were supplied by Qingdao Aoke Shimo Co. Ltd and Chloroauric acid was purchased from the Tianjin Yingda rare Chemical Reagent Plant. Concentrated phosphoric acid, concentrated sulfuric acid, potassium permanganate, hydrochloric acid (5%), hydrogen peroxide (30%), IPA and L-tryptophan were all obtained from the Tianjin Sailboat Chemical Reagent Co. Ltd. Concentrated nitric acid was provided by the Tianjin Kemiou Chemical Reagent Co., Ltd. Nitrogen was purchased from Tianjin Sixth Gas Co. Ltd, CEA and anti-CEA, serum, bovine serum albumin (BSA) and chitosan were all obtained from Shanghai Yuduo Biological Technology Co. Ltd. All chemicals used in this work were of analytical reagent grade and directly used without further purification. The water used was purified via a Millipore system ($\sim$18.2 MΩ cm).

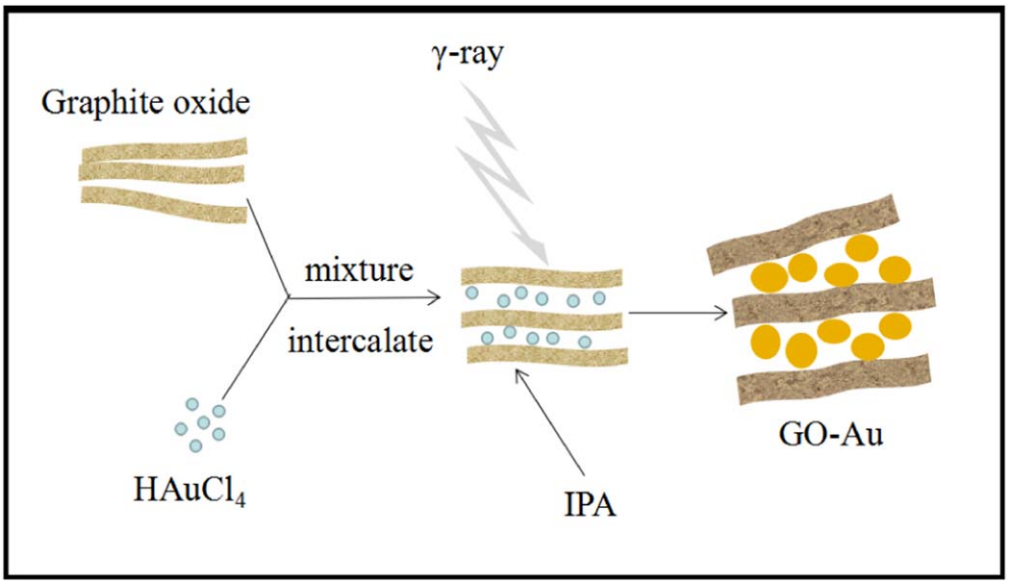

Scheme 1. Schematic illustration of the preparation process under γ irradiation and IPA.

2.2. Synthesis of GO

GO was obtained by the oxidation of natural graphite flakes using a modified Hummers method [20, 40–45]. In detail, H_3PO_4 (40 ml) and H_2SO_4 (360 ml) were mixed up together, and then 3 g of graphite and 18 g of $KMnO_4$ were simultaneously poured into it slowly in a water bath at 50 °C, stirring for 24 h. Afterwards, we poured the dark brown colloid mixture into the ice which was obtained by freezing the mixture of 400 ml H_2O and 3 ml H_2O_2, and then placed it at room temperature for 24 h. The supernatant was then removed and the gel left behind was washed with hydrochloric acid solution three to five times. After that, it was washed with deionized water by centrifugating at a speed of 10 000 rpm for 8 min several times until its pH was almost neutral. Finally, a small amount of the obtained yellow colloid was dried under vacuum for 24 h to calculate its solid content which was 5.7 mg g^{-1}.

2.3. Preparation of GO-Au nanocomposites

After diluting the graphite oxide solution containing 0.1 g of GO, the $HAuCl_4$ solution containing 0.4 mmol of solid $HAuCl_4$ was added, and followed by the addition of different amounts of IPA, the distilled water was added to it until the total volume was 100 ml, and then stirred at room temperature for 24 h. After that, the mixture was purged by N_2 for 30 min in order to remove the oxygen and then sealed. The suspensions were then exposed to a ^{60}Co γ-irradiation source to a dose of 150 kGy with a dose rate of 2.7 kGy h^{-1} at room temperature. After irradiation, the sample was removed from the γ-chamber and centrifuged at a speed of 10 000 rpm for 6 min with deionized water three times to remove the residuary impurity radicals. Lastly, the remaining product was freeze-dried with a condensing temperature of 223.15 K at an inside pressure of less than 20 Pa which provides us with the GO-Au nanocomposite powder samples. Then we marked the samples as Au0, Au1, Au2, Au3 and Au4 corresponding to the content ratio of IPA in the samples of 0/100, 1/100, 3/100, 5/100 and 7/100, respectively. The experimental procedure is shown in scheme 1. The γ-irradiation source used in this experiment was ^{60}Co γ-rays provided by the Beijing Hongyi Sifang Radiation Technology Co. Ltd with a ray radiation activity of 300 000 Curie.

2.4. Characterization

FTIR was measured using a Brook Vector-22 system. The samples were prepared with potassium bromide (KBr) powder and then were pressed into the translucent sheet. Raman spectra were recorded on a Renishaw in via Raman microscope with an excitation wavelength of 532 nm and a power of 1 mW. The XRD data were obtained by using the Bruker D8 Discover XRD with Cu Kα radiation (λ = 1.540 59 Å) at a scanning speed of 10°/min from 5 to 80°. XPS analyses were recorded on an Escalab 250 spectrometer (Thermo-VG Scientific, USA) to detect the surface atomic compositions (at%) of these composites. The morphology and nanostructure of the prepared samples were observed by HRTEM images taken in a JEM-2100 model instrument operated at 300 kV. Samples for HRTEM were prepared by introducing a drop of this diluted solution onto carbon-coated copper grids and allowed to dry in a desiccator.

All the electrochemical experiments were carried out in a three–electrode electrochemical cell system at room temperature. The CV test was used to detect the electrochemical behavior of the GO-Au samples to H_2O_2, and the test procedure is as follows: a glassy carbon (GC) electrode modified with the prepared samples and a platinum wire was used as the working and counter electrode, respectively. A silver/silver chloride (Ag/AgCl) electrode was used as the reference electrode. Then the electrodes were inserted into the hydrogen peroxide electrolyte and the volt-ampere characteristic scan curve was recorded. The catalytic performance of the

electrode was judged by the magnitude of the reduction peak current. For the CEA detection, the glassy carbon (GC) electrode modified with anti-CEA and a platinum wire were used as the working and counter electrode, respectively. A silver/silver chloride (Ag/AgCl) electrode was used as the reference electrode. Prior to modification, the GC electrode was polished with alumina slurry (0.05 μm) and cleaned in 0.1 M H2SO4 before potential cycling. The GO-Au nanocomposite modified GC electrode was fabricated by drop-casting 5 μl of an aqueous GO-Au solution and allowed to dry at room temperature for an hour. This GO-Au modified electrode was used for electrochemical sensing of H2O2. Then the anti-CEA was dropped in the electrode modified with the Au0 sample for electrochemical immunosensing of CEA. All the electrochemical measurements were carried out by using a CHI-660D electrochemical workstation. A 0.1 mol l^{-1} phosphate buffer solution (PBS) (pH 7.2) was used as a supporting electrolyte for electrochemical experiments and all the potentials were quoted against the Ag/AgCl reference electrode unless otherwise mentioned.

3. Results and discussion

3.1. Morphology and microcrystalline structure of GO-Au nanocomposites

FTIR spectra showed the changes of functional groups on the various samples of GO-Au nanocomposites. As shown in figure 1(a), there were significant peaks at different positions in the profile of the Au0 sample: the broad band observed at around 3452 cm^{-1} and the sharp peak at 1415 cm^{-1} were ascribed to the stretching and bending vibration of OH groups produced by water molecules that were absorbed on GO; the weaker peaks at 2924 cm^{-1} and 2855 cm^{-1} correspond to the antisymmetric stretching vibration and symmetrical stretching vibration of C–H bonding out-plane, and the peak at 1381 cm^{-1} was the cause of bending vibrations of C–H bonding in-plane; the peak displayed in 1739 cm^{-1} was in accordance with the stretching vibration of C=O bonding of carboxyl and carbonyl groups; and the stronger peak at 1628 cm^{-1} was associated with the stretching vibration of C=C bonding; the peak at 1066 cm^{-1} was due to the stretching vibration of C–O and C–O–C groups. Figure 1(a) shows that the Au0 sample had the highest oxidation degree, while with the increasing addition of IPA solution, the oxygen-containing groups decreased significantly due to the reducing property of isopropyl radicals in the system and the γ-radiolysis process. Then after 7 ml of IPA was added into the reaction system (Au4), we can hardly see the obvious peak of oxygen-containing groups which means the content of IPA was adequate to eliminate the oxygen-containing groups on GO. The reaction mechanism was deduced by the following text. At first, there would be some preliminary radicals such as e^-_{aq}, H·, ·OH in the solution produced by γ-radiolysis of the water [16]. The e^-_{aq} and H · are reducing in nature while the ·OH is oxidative. Then the abundant precursor of $HAuCl_4$ intercalated in the GO solution were reduced to elemental gold by the reducing radicals produced by the γ-irradiation of water. Afterwards, the rapidly agglomerated AuNPs due to their high surface energy can be divided to smaller AuNPs by the fragmentation capability of high-energy γ-rays while there is absence of IPA in the reaction system (Au0). Then we added different amount of IPA to the radiolysis system. The IPA acted as the free-radical scavenger for ·OH, can react with the ·OH to form isopropyl radicals which are reductive in essence in the anaerobic condition and provide a reducing environment for the reaction [17]. Under the same absorbed dose rate of γ-rays, the amount of isopropyl radicals can increase with the increasing additive of IPA, thus the reaction system of different samples was more reductive which can not only reduce the gold ions to a zero-valent state but also reduce the GO to a certain degree.

The chemical reactions taking place in the mixture are as follows:

$$\text{n.}H_2O\ (\text{radiolysis}) \rightarrow e^-_{aq},\ H\cdot,\cdot OH,\ H^+,\ H_2O_2,\ \ldots\ \text{etc.} \quad (1)$$

$$(CH_3)_2CHOH + \cdot OH \rightarrow (CH_3)_2C\cdot OH + H_2O. \quad (2)$$

$$\text{GO} + \text{reducing radicals}\ (e^-_{aq},\ (CH_3)_2C\cdot OH,\ H\cdot,\ \ldots\ \text{etc}) \rightarrow \text{reduced GO}. \quad (3)$$

$$Au^{3+} + \text{reducing radicals}\ (e^-_{aq},\ (CH_3)_2C\cdot OH,\ H\cdot,\gamma\ \text{radiolysis},\ \ldots\ \text{etc}) \rightarrow \text{AuNPs}. \quad (4)$$

The crystalline structure of these GO-Au nanocomposites is presented in the XRD image in figure 1(b). It can be observed that the profile of Au0 exhibited an obvious sharp peak at 10.15° which corresponds to the C (001) plane of GO. Then with the increasing addition of IPA, the peak becomes weaker and even vanished at 10.15° while broad peaks appeared around 24° which indicated that the GO had been reduced. Also, in addition to the peak of reduced GO, another four significant diffraction peaks appear at 37.96°, 44.05°, 64.28° and 77.33° ascribed to the (111) (200) (220) and (311) facets of Au elements, respectively, which provided direct evidence that the AuNPs with face central cubic structure has successfully formed in the composites. The size of AuNPs were calculated with the Debye–Scherrer equation, which turned out to be 3.514 nm, 3.528 nm, 3.544 nm, 3.551 nm and 3.533 nm corresponding to the samples of Au0, Au1, Au2, Au3 and Au4, respectively.

Raman spectra of GO-Au nanocomposites were shown in figure 1(c) and the value of I_D/I_G was displayed in figure 1(d). The Raman spectra of GO-Au nanocomposites exhibited a prominent D band at around 1347 cm^{-1} which corresponds to the in-plane vibration of sp^2 hybrid carbon atoms as well as a highlighted G peak at about 1589 cm^{-1} which was due to the carbon atoms with dangling bonds in-plane terminations and the results can represent the amount of disorder and relative degree of graphitization, respectively [46]. The ratio of I_D/I_G can reflect the degree of disorders or area of sp^2 domains of GO [16]. Compared with the 0.89 of the I_D/I_G value of Au0, the ratio of I_D/I_G of Au1, Au2 and Au3 samples were increased to 0.96, 0.98 and 1.09,

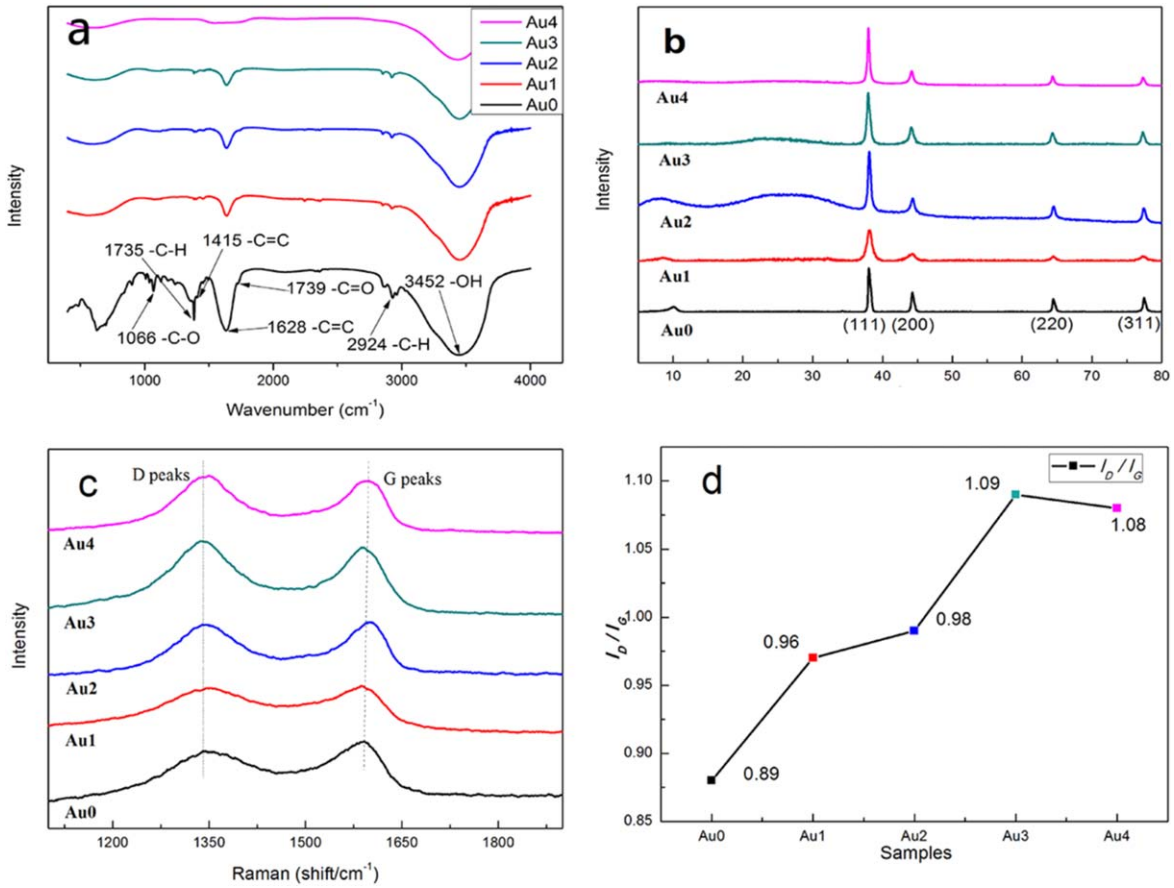

Figure 1. (a) FTIR spectra of GO-Au composites prepared with different content of IPA; (b) XRD diffraction patterns of GO-Au composites; (c) Raman spectra of GO-Au composites; (d) the trend of I_D/I_G value from Raman spectra of GO-Au nanocomposites.

Table 1. Analysis of the deconvoluted C1s peaks from XPS of the prepared composites.

Samples B.E(eV)	Sp2 C–C (%) 284.0–284.4	Sp3 C–C (%) 284.5–285.1	C–OH (%) 286.2–286.7	C–O–C (%) 286.8–287.3	C=O (%) 287.5–288.2	–COOH (%) 288.5–289	sp^2 C–C/sp^3 C–C —
Au0	16.85	33.7	16.85	13.48	14.61	4.51	0.5
Au1	25	37.5	14.94	10.19	7.69	4.69	0.667
Au2	30.61	40.82	10.49	8.20	5.52	4.36	0.750
Au3	38.59	38.59	8.80	6.76	4.26	3.01	1
Au4	37.21	41.80	8.04	6.26	3.83	2.86	0.890

separately. The trend indicated that the I_D/I_G value was positively correlated with the concentration of IPA which meant the defects and the reduction degree of GO were rising with the increasing of IPA amount [47]. With the further increasing of the additive amount of IPA (7 ml), the I_D/I_G value decreased (to 1.08), which was regarded as the increase of defects on GO [48], the AuNPs reduced by IPA and γ-irradiation covered the defects of GO and it also proved the AuNPs were embedded in the interlayer of GO and that the oxygen-containing groups in the GO have a great degree of reduction while the addition of IPA up to 5 ml in the system hence the IPA content was excess.

Figures 2(a)∼(e) showed the C1s spectra fitted by a Gaussiane–Lorentzian peak shape, and the detailed information about the functional groups on the prepared composites was displayed in table 1. It can be observed that the value of sp^2 C–C/sp^3 C–C ratio exhibited a trend of increase first (Au0 to Au3) and then descended (to Au4), which meant the degree of graphitization on the GO was the opposite tendency. The results were in highly consistent with the Raman spectra (figure 1(c) and (d)). It also proved that the level of all kinds of oxygen-containing groups showed a decreasing trend with the increasing additive of IPA in table 1. The oxygen-containing groups reduced a little while the addition of IPA increased from 5 ml to 7 ml, which indicated that the additive amount of IPA was adequate. Furthermore, the table 2 demonstrated that the amount of oxygen element reduced sharply after the addition of IPA. Moreover, the figure 2(f) also convincingly proved that the AuNPs were grown in the GO, and all the gold elements existed in the form of an

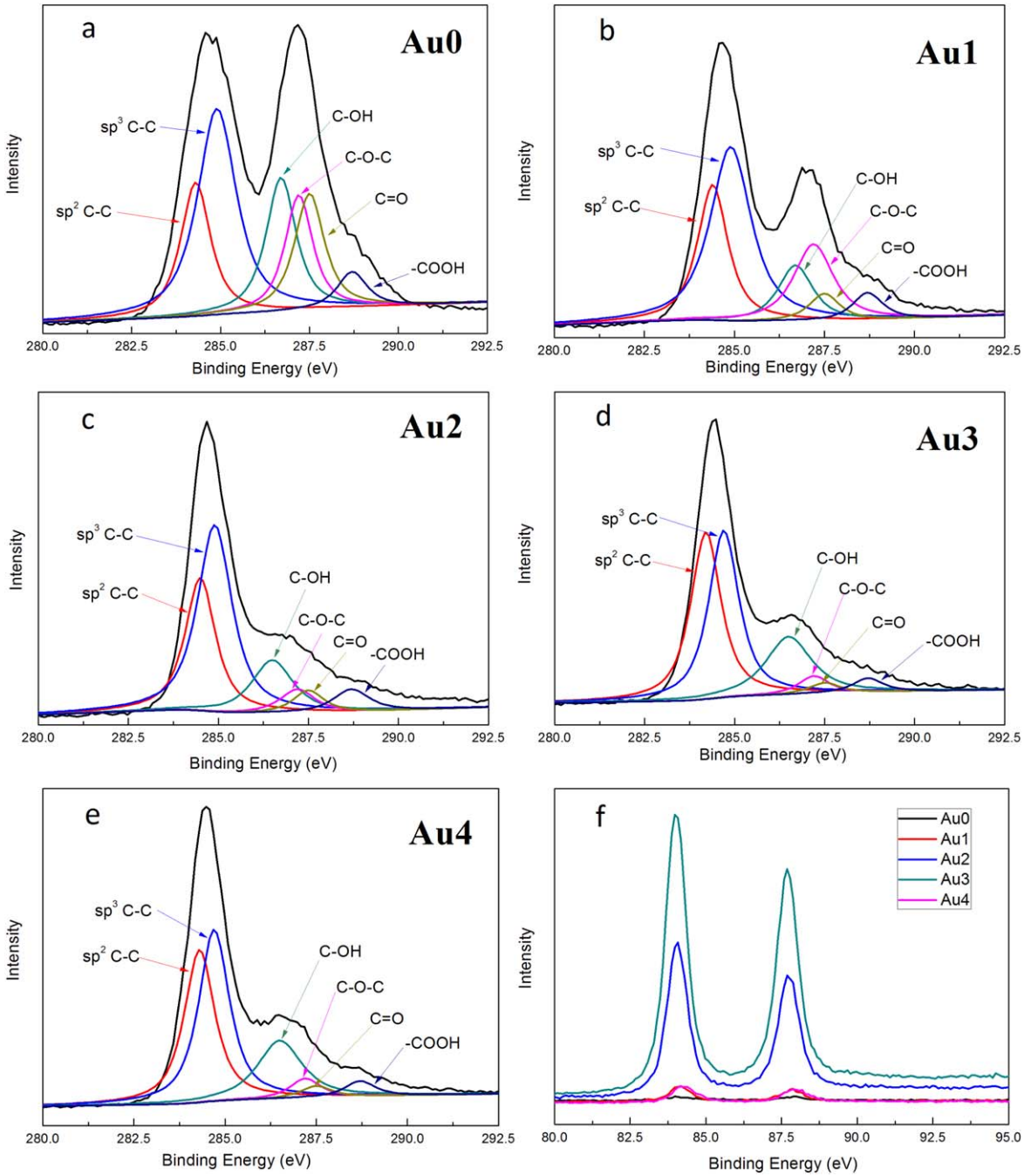

Figure 2. C1s XPS spectra of Au0 (a), Au1 (b), Au2 (c), Au3 (d) and Au4 (e) samples;(f) XPS peaks of Au 1s in different samples.

elementary substance rather than compounds. Additionally, it can be observed that the content of AuNPs in the surface of various samples showed an increasing trend from Au0 to Au3, and then reduced in Au4 with the decrease of oxygen-containing groups.

The HRTEM images of the GO-Au composites are shown in figure 3. The mean size of these samples were 3.09, 3.33, 3.54, 3.69 and 3.53 nm of Au0, Au1, Au2, Au3 and Au4, respectively. It showed an interesting phenomenon that the size of the AuNPs on the GO displayed an increasing trend from Au0 to Au3 while being smaller in Au4 with the increasing addition of IPA and the trends were in accordance with the results calculated by XRD spectra. Figure 3(f) showed the Fourier transform diagrams at different locations on the GO-Au composites and the AuNPs with a single crystalline structure are indicated by the regularly dotted pattern and well-resolved lattice fringes. The lattice of GO and the AuNPs grown on the surface of GO showed a regular six-membered ring shape (f2) and a parallelogram shape (f1), respectively. The bright irregular circular ring indicated that

Table 2. The ratio of C/O in various samples.

Samples	Au0	Au1	Au2	Au3	Au4
Ratio	2.39	3.02	4.05	4.32	4.56

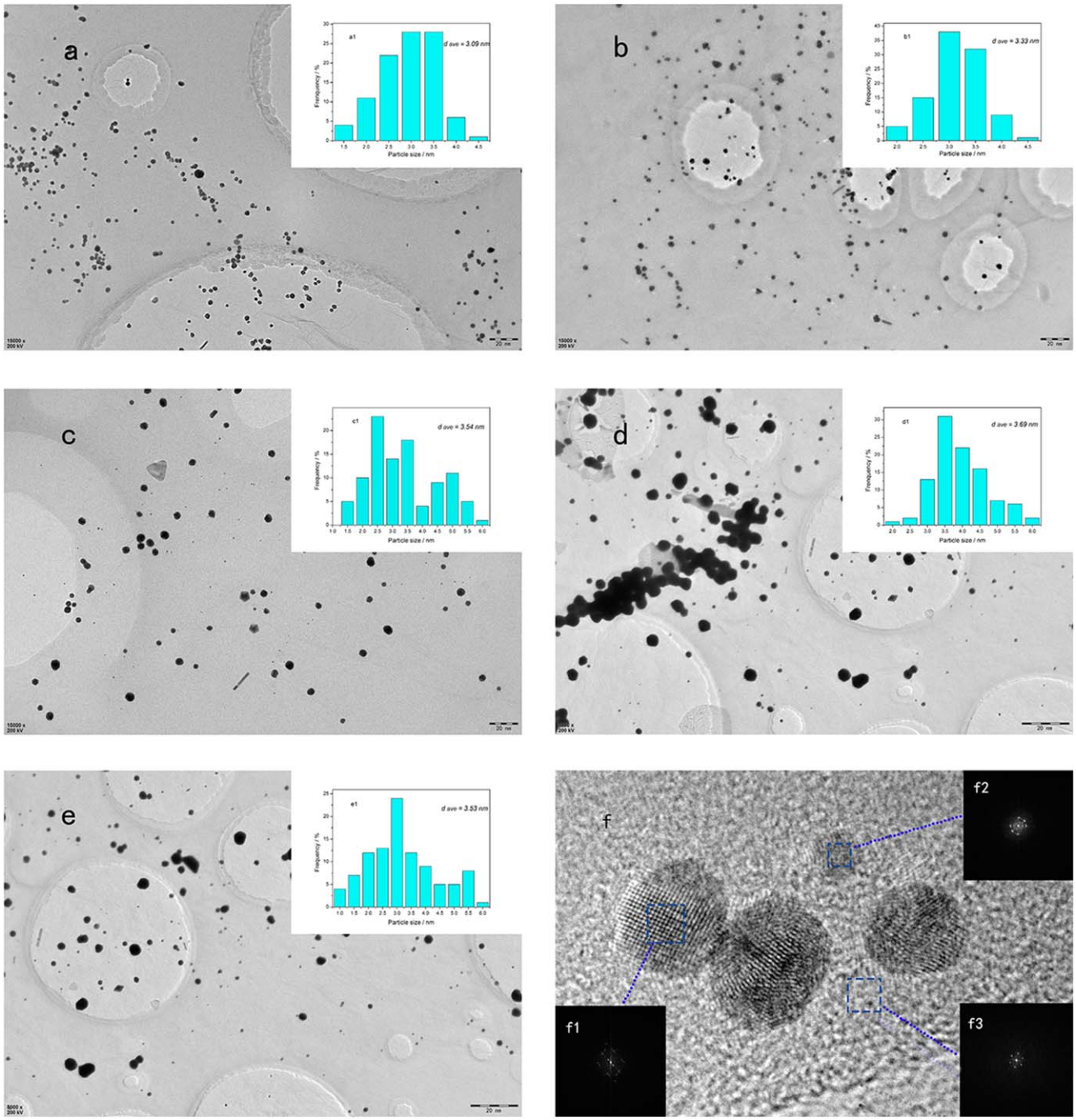

Figure 3. HRTEM images of GO-Au composites in the scale bar of 20 nm: (a) Au0, (b) Au1, (c) Au2, (d) Au3, (e) Au4; Inset: the size distribution histogram of the corresponding TEM image of the GO-Au composites; (f) Fourier transform diagrams at different locations on the GO-Au composites.

the AuNPs were intercalated in the sheets of GO which means that the AuNPs were between the GO layer. To better understand the dispersion mechanism of AuNPs in GO under IPA and γ-irradiation process, we should first find the differences between the prepared five samples. The FTIR image (figure 1(a)) combined with the HRTEM figures suggested that the lower the amount of oxygen-containing groups, the larger the size of the AuNPs and more uniform the dispersion was at first, and then the size of AuNPs become a little smaller while the oxygen-containing groups reduced to a certain degree. This phenomenon confirmed that the oxygen-containing groups played a non-negligible role in the dispersion mechanism of AuNPs on GO during the γ-irradiation process for biosensors. And as we all know, hydroxyl and epoxide are distributed on the basal plane of GO while the carbonyl and carboxyl are located on the edges of GO, so that we can infer that the distribution of AuNPs in the GO is more likely related to the hydroxyl and epoxide. As we can see, the AuNPs in figure 3(a) were small in size and distributed uniformly, and then with the decreasing levels of hydroxyl and

epoxide, the AuNPs in the prepared samples became large and have a certain degree of reunion. This result illustrated that there might exist a negative correlation between the amount of oxygen-containing groups with the size of AuNPs during the γ-irradiation process, thus we inferred that the hydroxyl and epoxide between the neighboring GO layers can exert a capture effect in order to catch the AuNPs which promotes a more even distribution of AuNPs. On the basis of these results, we suspected the growth mechanism of AuNPs in the GO during γ-irradiation process was by the following inference. Under the synergistic effect of γ-irradiation and IPA, Au ions were reduced to elemental gold, and then trapped by hydroxyl and epoxide on the GO. Afterwards, the gold element acted as the crystal nucleus, and other Au particles began to grow and adhere to it. As a result, the high amount of oxygen-containing groups endow more AuNPs growing in the GO layers and then the further growth of AuNPs would be controlled by the γ-irradiation. Afterwards, the content of oxygen-containing groups reduced with the increasing addition of IPA, which provided more space for the sufficient growth of the produced Au crystal grains. Therefore, the size of AuNPs became large as the amount of hydroxyl and epoxide decreases. When the content of oxygen-containing groups had been reduced to a certain extent, the distance between the GO sheets became smaller, thus limiting the further growth of AuNPs.

Therefore, we suspected the mechanism on the growth of AuNPs on GO to be by the following deduction. At first, while there was absence of IPA or little IPA in the reaction system, the Au^{3+} was reduced to Au mainly by the reducing radicals produced during the γ-radiolysis process, and these radicals were in a weak reduction which can only reduce the metal ions rather than the oxygen-containing groups on the GO. This way, the growth of AuNPs could be restricted by the fragmentation ability of γ-irradiation. Then, with the increasing addition of IPA in the system, these reducing radicals produced in the γ-radiolysis process could not only reduce the Au^{3+} but also the oxygen-containing groups on the GO, which would in turn weaken the van der Waals' force and increased the interlayer spacing of the GO. Thus the growth of AuNPs on GO would be controlled by the effect of the content of oxygen-containing groups and the interlamellar limitation of GO, that is, during the γ-irradiation process, when there are large numbers of the hydroxyl and epoxide, oxygen-containing groups played a major role in the growth of AuNPs, and while they were reduced to a certain extent, the interlamellar confinement effect of GO started to exert an influence on the size of AuNPs.

3.2. Performance of the prepared GO-Au nanocomposites

Since the electrocatalytic activity of the GO-Au nanocomposites dominates the sensitivity of the fabricated electrochemical immunosensor, we need to detect the signal amplification capability of these samples. As H_2O_2 is an extensively existing chemical in living bodies which can be catalyzed by Au elements, it was used in detecting the electrocatalytic activity of the GO-Au nanocomposites. Thus we detect the electrocatalytic activity of the GO-Au nanocomposites to H_2O_2 before we determine the immunosensor performance to CEA. As figure 4(a) and (b) show, the electrochemical immunosensor performance gradually decreases from Au0 to Au3, and then increases from Au3 to Au4 as the amount of IPA addition in the samples during the experiment process increases. In a word, the results indicated that the smaller the gold particle size and the higher degree of graphitization, the stronger the catalytic response to H_2O_2 was. The catalytic property of the prepared samples was promoted by the synergistic effect of the size of the metal particles and the degree of graphitization, as the small particle size can provide a large catalytic surface area and the complete graphite structure offers many electron transport channels [48]. Meanwhile, on the basis of figure 2(f), it can be observed that the Au0 sample with smallest particle size had the lowest relative amount of Au particles but showed the best catalytic property of all the five samples, which meant the highest utilization of the gold elements in the Au0 sample. In addition, it also proved that the effect of the prepared composites structure on the biosensor performance of GO-Au nanocomposites is very significant. Consequently, as the Au0 sample exhibited an excellent electrocatalytic activity for H_2O_2, it was chosen to further detect the sensitivity of the immunosensor for CEA [12].

The Au0 sample was coated in the glassy carbon electrode and then modified with anti-CEA, which endowed it with the special selectivity to CEA. We then investigated the immunosensor performance to CEA by SWV tests, which were recorded with 0 V–0.3 V in 0.1 mol $\cdot$ l^{-1} PBS and 0.3 M H_2O_2 at a 0.05 V s^{-1} scan rate by the electrochemical workstation. During the test process, CEA with different concentrations were added into the electrolyte and the SWV current response at around 0.7 V was recorded while each 1 ng of CEA was added. As the blocking effect of antigen-antibody loaded on the Au0 sample modified the GCE, the degree of electron transfer (generated during the catalytic reduction process of H_2O_2 by Au) would be limited and thus the redox current lessened as the concentration of CEA increased. The reduction in redox current is displayed in the inset of figure 4(c). From figure 4(c), the peak intensity of the SWV curves was negatively correlated with the concentration of CEA. The Au0 sample modified with anti-CEA and CEA showed the SWV response at around 0.13 V and exhibited a low detection limit of 15.8 pg ml^{-1} ($S/N = 3$) and a wider linear range from 1 to 40 ng ml^{-1}, and this performance belonged to a medium grade level compared to other carbon-based precious metal biosensors for CEA which were prepared in more complicated methods according to the table 3.

The selectivity of the electrode modified with the Au0 sample and anti-CEA was conducted subsequently and the result could be observed in figure 4(d). To evaluate the selectivity of the Au0 immunosensor for CEA, various potentially interfering substances were added during the CEA detection. During the detection process, 10 ng CEA were added into the electrolyte and the peak current of SWV response were recorded. Then L-tryptophan, BSA and chitosan of 500 ng were chosen as the interference factors added

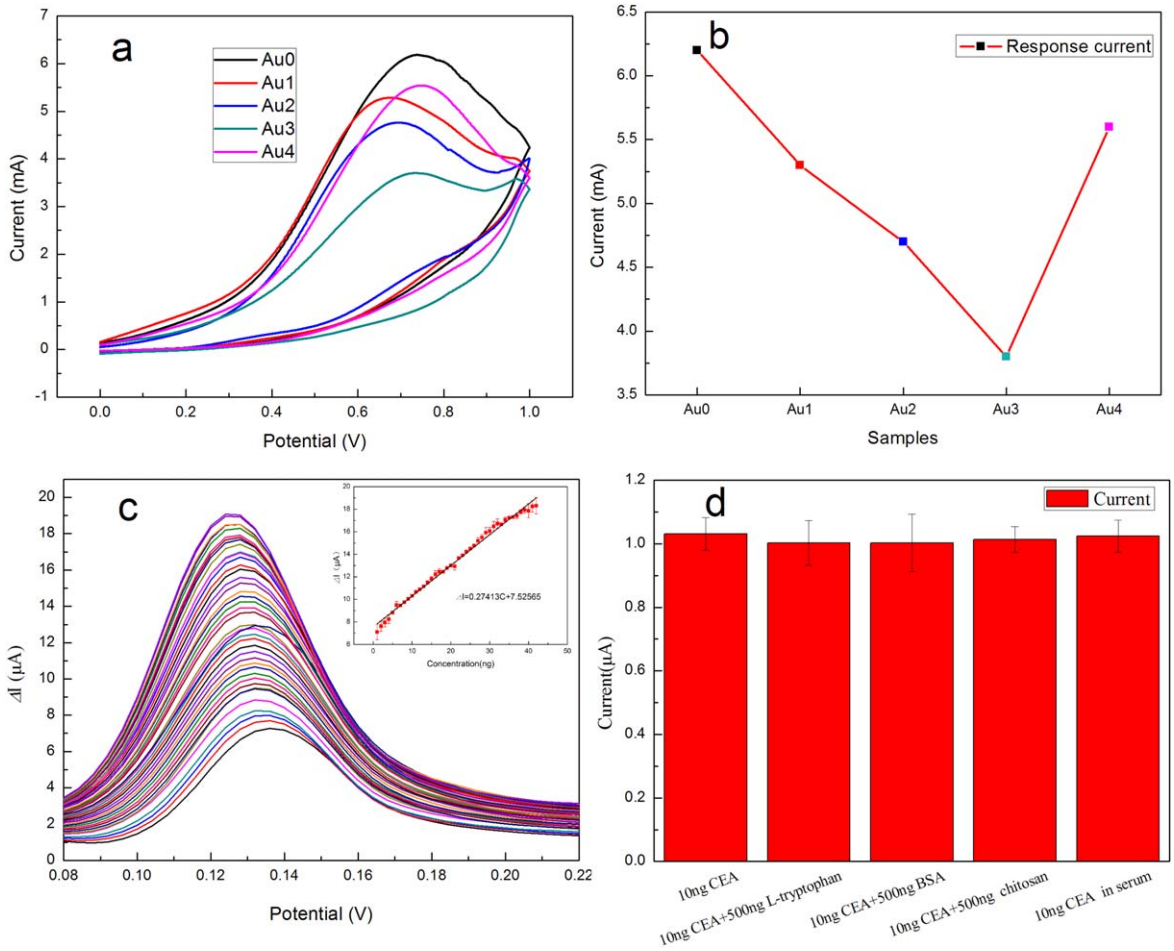

Figure 4. CV recorded for GO-Au composites with H_2O_2 (a) and the trend of maximum response current of CV (b); (c) SWV recorded of Au0 sample. Inset: fitted plot of peak current versus concentration of CEA; (d) The selectivity of the electrode modified with the as-prepared composites of Au0 samples and anti-CEA.

Table 3. Comparison of the performance of electrochemical sensors in detecting cancer cell-related substances with previous work.

Materials	Detection object	Limit of Detection	Reference
AuNPs-TiO_2-graphene nanocomposite	CEA	10 ng ml^{-1}	[49]
Thionine monolayer modified gold	CEA	200 pg ml^{-1}	[50]
AuNPs and graphene	CEA	280 pg ml^{-1}	[51]
Immuno-magnetic bead	CEA	500 pg ml^{-1}	[52]
AuPt nanochains on MWCNTS	CEA	38 ng ml^{-1}	[2]
Graphene quantum dots and Au@Pt	CEA	6 pg ml^{-1}	[53]
Ag/Au nanoparticles coated graphene	CEA	8 pg ml^{-1}	[54]
AuNPs-aptamer-UCNPs sandwich complex	CEA	0.5 ng ml^{-1}	[55]
Graphene-Au nanoparticles	CEA	15.8 pg ml^{-1}	This work

into the electrolyte and the SWV response were recorded. Additionally, 10 ng CEA was put into the real human serum and then the change in current response was compared. The results exhibited that the current response in the immune reaction process was almost undisturbed which demonstrated that the Au0 sample with anti-CEA showed a high selectivity to CEA. The selectivity test also manifested that the GO-Au samples prepared with γ-irradiation applied in a biosensor are viable. It can also offer a promising potential application in the detection of other biomolecules when modified with the corresponding antigen or antibody.

4. Conclusions

In this work, the GO structure evolution and interlayer-embedded Au nanoparticle size and dispersion induced from γ-ray and IPA for biosensors were investigated. AuNPs were

in situ formed in GO interlayers and the prepared sample demonstrated excellent performance for CEA detection with a low detection limit of 15.8 pg ml^{-1} and a high selectivity when modified with an anti-CEA. Results show that the greater content of oxygen-containing groups and higher degree of graphitezation on the GO determined the smaller size and more uniform distribution of AuNPs on GO and thus lead to a better electrochemical immunosensor performance of the GO-Au nanocomposites. The small size and uniform dispersion of AuNPs was attributed to the synergistic effect of γ-irradiation, content of oxygen-containing groups and the interlamellar confinement of GO. This work extends the approaches for fabricating GO-Au nanocomposites as efficient immunosensors to CEA, and we could further optimize the immunosensor performance by regulating the structure of the GO.

Acknowledgments

The work was funded by the National Natural Science Foundation of China (11575126) and Science & Technology Development Fund of Tianjin Education Commission for Higher Education (2018KJ194).

ORCID iDs

Zhiwei Xu https://orcid.org/0000-0002-8067-5344

References

[1] Wang Y, Wang Y, Wu D, Ma H, Zhang Y, Fan D, Pang X, Du B and Wei Q 2018 Label-free electrochemical immunosensor based on flower-like Ag/MoS_2/rGO nanocomposites for ultrasensitive detection of carcinoembryonic antigen *Sensors Actuators* B **255** 125–32

[2] Lu W, Ge J, Tao L, Cao X, Dong J and Qian W 2014 Large-scale synthesis of ultrathin Au-Pt nanowires assembled on thionine/graphene with high conductivity and sensitivity for electrochemical immunosensor *Electrochim. Acta* **130** 335–43

[3] Lv H, Li Y, Zhang X, Gao Z, Feng J, Wang P and Dong Y 2018 The label-free immunosensor based on rhodium@palladium nanodendrites/sulfo group functionalized multi-walled carbon nanotubes for the sensitive analysis of carcino embryonic antigen *Anal. Chim. Acta* **1007** 61–70

[4] Wang Y, Zhao G, Zhang Y, Pang X, Cao W, Du B and Wei Q 2018 Sandwich-type electrochemical immunosensor for CEA detection based on Ag/MoS_2@Fe_3O_4 and an analogous ELISA method with total internal reflection microscopy *Sensors Actuators* B **266** 561–9

[5] Qin Z, Xu W, Chen S, Chen J, Qiu J F and Li C R 2018 Electrochemical immunoassay for the carcinoembryonic antigen based on the use of a glassy carbon electrode modified with an octahedral Cu_2O-gold nanocomposite and staphylococcal protein for signal amplification *Mikrochim. Acta* **185** 266

[6] Luan C, Xu Y, Chen B and Yang Z 2017 Responsive photonic encoded breathing microbeads based microfluidic chip for multiplex fluorescent immunoassay *Sensors Actuators* B **242** 1259–64

[7] Song E, Han W, Li J, Jiang Y, Cheng D, Song Y, Zhang P and Tan W 2014 Magnetic-encoded fluorescent multifunctional nanospheres for simultaneous multicomponent analysis *Anal. Chem.* **86** 9434–42

[8] Zong C, Wu J, Wang C, Ju H and Yan F 2012 Chemiluminescence imaging immunoassay of multiple tumor markers for cancer screening *Anal. Chem.* **84** 2410–5

[9] Pei X, Chen B, Li L, Gao F and Jiang Z 2010 Multiplex tumor marker detection with new chemiluminescent immunoassay based on silica colloidal crystal beads *Analyst* **135** 177–81

[10] Rashidiani J, Kamali M, Sedighian H, Akbariqomi M, Mansouri M and Kooshki H 2018 Ultrahigh sensitive enhanced-electrochemiluminescence detection of cancer biomarkers using silica NPs/graphene oxide: a comparative study *Biosens. Bioelectron.* **102** 226–33

[11] Rizwan M, Elma S, Lim S A and Ahmed M U 2018 AuNPs/CNOs/SWCNTs/chitosan-nanocomposite modified electrochemical sensor for the label-free detection of carcinoembryonic antigen *Biosens. Bioelectron.* **107** 211–7

[12] Chen Y, Li Y, Deng D, He H, Yan X, Wang Z, Fan C and Luo L 2018 Effective immobilization of Au nanoparticles on TiO_2 loaded graphene for a novel sandwich-type immunosensor *Biosens. Bioelectron.* **102** 301–6

[13] Chen Z, Zhang C, Li X, Ma H, Wan C, Li K and Lin Y 2015 Aptasensor for electrochemical sensing of angiogenin based on electrode modified by cationic polyelectrolyte-functionalized graphene/gold nanoparticles composites *Biosens. Bioelectron.* **65** 232–7

[14] Xu S, Zhang R, Zhao W, Zhu Y, Wei W, Liu X and Luo J 2017 Self-assembled polymeric nanoparticles film stabilizing gold nanoparticles as a versatile platform for ultrasensitive detection of carcino-embryonic antigen *Biosens. Bioelectron.* **92** 570–6

[15] Wang M, Zhang S, Song Y, Dong J, Wei H, Xie H, Fang X, Shao L, Huang Y and Jiang Z 2016 Fabrication of light, flexible and multifunctional graphene nanoribbon fibers via a 3D solution printing method *Nanotechnology* **27** 465702

[16] Yue Y, Zhou B, Shi J, Chen C, Li N, Xu Z, Liu L, Kuang L, Ma M and Fu H 2017 γ-Irradiation assisted synthesis of graphene oxide sheets supported Ag nanoparticles with single crystalline structure and parabolic distribution from interlamellar limitation *Appl. Surf. Sci.* **403** 282–93

[17] Hareesh K, Joshi R P, Dahiwale S S, Bhoraskar V N and Dhole S D 2016 Synthesis of Ag-reduced graphene oxide nanocomposite by gamma radiation assisted method and its photocatalytic activity *Vacuum* **124** 40–5

[18] Jiang Z *et al* A high efficiency H2S gas sensor material: paper like Fe_2O_3/graphene nanosheets and structural alignment dependency of device efficiency *J. Mater. Chem.* A **2** 2014 6714–7

[19] Zhang Y, Shi J, Chen C, Li N, Xu Z, Liu L, Zhao L, Li J and Jing M 2018 Structural evolution of defective graphene under heat treatment and gamma irradiation *Physica* E **97** 151–4

[20] Kang H, Shi J, Liu L, Shan M, Xu Z, Li N, Li J, Lv H, Qian X and Zhao L 2018 Sandwich morphology and superior dye-removal performances for nanofiltration membranes self-assemblied via graphene oxide and carbon nanotubes *Appl. Surf. Sci.* **428** 990–9

[21] Jiang W, Wang H, Xu Z, Li N, Chen C, Li C, Li J, Lv H, Kuang L and Tian X 2018 A review on manifold synthetic and reprocessing methods of 3D porous graphene-based architecture for Li-ion anode *Chem. Eng. J.* **335** 954–69

[22] Jia Z, Ben Amar M, Yang D, Brinza O, Kanaev A, Duten X and Vega-González A 2018 Plasma catalysis application of gold nanoparticles for acetaldehyde decomposition *Chem. Eng. J.* **347** 913–22

[23] Zhou J, Gan N, Li T, Zhou H, Li X, Cao Y, Wang L, Sang W and Hu F 2013 Ultratrace detection of C-reactive protein by a piezoelectric immunosensor based on Fe_3O_4@SiO_2 magnetic capture nanoprobes and HRP-antibody co-immobilized nano gold as signal tags *Sensors Actuators* B **178** 494–500

[24] Guner A, Cevik E, Senel M and Alpsoy L 2017 An electrochemical immunosensor for sensitive detection of *Escherichia coli* O157:H7 by using chitosan, MWCNT, polypyrrole with gold nanoparticles hybrid sensing platform *Food Chem.* **229** 358–65

[25] Khashayar P, Amoabediny G, Larijani B, Hosseini M and Vanfleteren J 2017 Fabrication and verification of conjugated AuNP-antibody nanoprobe for sensitivity improvement in electrochemical biosensors *Sci. Rep.* **7** 16070

[26] Lin C-H, Wu C-C and Kuo Y-F 2016 A high sensitive impedimetric salbutamol immunosensor based on the gold nanostructure-deposited screen-printed carbon electrode *J. Electroanal. Chem.* **768** 27–33

[27] Yang C, Wang Q, Xiang Y, Yuan R and Chai Y 2014 Target-induced strand release and thionine-decorated gold nanoparticle amplification labels for sensitive electrochemical aptamer-based sensing of small molecules *Sensors Actuators* B **197** 149–54

[28] Alizadeh N, Salimi A and Hallaj R 2018 Magnetoimmunosensor for simultaneous electrochemical detection of carcinoembryonic antigen and α-fetoprotein using multifunctionalized Au nanotags *J. Electroanal. Chem.* **811** 8–15

[29] Jeon E K, Seo E, Lee E, Lee W, Um M K and Kim B S 2013 Mussel-inspired green synthesis of silver nanoparticles on graphene oxide nanosheets for enhanced catalytic applications *Chem Commun (Camb)* **49** 3392–4

[30] Mao A, Zhang D, Jin X, Gu X, Wei X, Yang G and Liu X 2012 Synthesis of graphene oxide sheets decorated by silver nanoparticles in organic phase and their catalytic activity *J. Phys. Chem. Solids* **73** 982–6

[31] Bai W, Nie F, Zheng J and Sheng Q 2014 Novel silver nanoparticle-manganese oxyhydroxide-graphene oxide nanocomposite prepared by modified silver mirror reaction and its application for electrochemical sensing *ACS Appl. Mater. Interfaces* **6** 5439–49

[32] Shan M, Wang H, Xu Z, Li N, Chen C, Shi J, Liu L, Kuang L, Ma M and Zhang C 2018 Synergetic improvement of mechanical properties and surface activities in [gamma]-irradiated carbon fibers revealed by radial positioning spectroscopy and mechanical model *Anal. Methods* **10** 496–503

[33] Wang H, Teng K, Chen C, Li X, Xu Z, Chen L, Fu H, Kuang L, Ma M and Zhao L 2017 Conductivity and electromagnetic interference shielding of graphene-based architectures using MWCNTs as free radical scavenger in gamma-irradiation *Mater. Lett.* **186** 78–81

[34] Zhu T, Teng K, Shi J, Chen L and Xu Z 2016 A facile assembly of 3D robust double network graphene/polyacrylamide architectures via γ-ray irradiation *Compos. Sci. Technol.* **123** 276–85

[35] Sui X, Xu Z, Hu C, Chen L, Liu L, Kuang L, Ma M, Zhao L, Li J and Deng H 2016 Microstructure evolution in γ-irradiated carbon fibers revealed by a hierarchical model and Raman spectra from fiber section *Compos. Sci. Technol.* **130** 46–52

[36] Zhao X, Li N, Jing M, Zhang Y, Wang W, Liu L, Xu Z, Liu L, Li F and Wu N 2019 Monodispersed and spherical silver nanoparticles/graphene nanocomposites from gamma-ray assisted *in situ* synthesis for nitrite electrochemical sensing *Electrochim. Acta* **295** 434–43

[37] Li X, Liu L, Xu Z, Wang W, Shi J, Liu L, Jing M, Li F and Zhang X 2019 Gamma irradiation and microemulsion assisted synthesis of monodisperse flower-like platinum-gold nanoparticles/reduced graphene oxide nanocomposites for ultrasensitive detection of carcinoembryonic antigen *Sensors Actuators* B **287** 267–77

[38] Jiang K, Huang Q, Fan K, Wu L, Nie D, Guo W, Wu Y and Han Z 2018 Reduced graphene oxide and gold nanoparticle composite-based solid-phase extraction coupled with ultra-high-performance liquid chromatography-tandem mass spectrometry for the determination of 9 mycotoxins in milk *Food Chem.* **264** 218–25

[39] Peng D, Liang R-P, Huang H and Qiu J-D 2016 Electrochemical immunosensor for carcinoembryonic antigen based on signal amplification strategy of graphene and Fe_3O_4/Au NPs *J. Electroanal. Chem.* **761** 112–7

[40] Zhang J, Xu Z, Shan M, Zhou B, Li Y, Li B, Niu J and Qian X 2013 Synergetic effects of oxidized carbon nanotubes and graphene oxide on fouling control and anti-fouling mechanism of polyvinylidene fluoride ultrafiltration membranes *J. Membr. Sci.* **448** 81–92

[41] Xu Z, Zhang J, Shan M, Li Y, Li B, Niu J, Zhou B and Qian X 2014 Organosilane-functionalized graphene oxide for enhanced antifouling and mechanical properties of polyvinylidene fluoride ultrafiltration membranes *J. Membr. Sci.* **458** 1–13

[42] Wang L, Guo H, Wang W, Teng K, Xu Z, Chen C, Li C, Yang C and Hu C 2016 Preparation of sandwich-like phosphorus/reduced graphene oxide composites as anode materials for lithium-ion batteries *Electrochim. Acta* **211** 499–506

[43] Zhang J, Xu Z, Mai W, Min C, Zhou B, Shan M, Li Y, Yang C, Wang Z and Qian X 2013 Improved hydrophilicity, permeability, antifouling and mechanical performance of PVDF composite ultrafiltration membranes tailored by oxidized low-dimensional carbon nanomaterials *J. Mater. Chem.* A **1** 3101–11

[44] Li W, Xu Z, Chen L, Shan M, Tian X, Yang C, Lv H and Qian X 2014 A facile method to produce graphene oxide-g-poly(L-lactic acid) as an promising reinforcement for PLLA nanocomposites *Chem. Eng. J.* **237** 291–9

[45] Xu Z, Wu T, Shi J, Teng K, Wang W, Ma M, Li J, Qian X, Li C and Fan J 2016 Photocatalytic antifouling PVDF ultrafiltration membranes based on synergy of graphene oxide and TiO_2 for water treatment *J. Membr. Sci.* **520** 281–93

[46] Rahimi A, Zanjanchi M A, Bakhtiari S and Dehsaraei M 2018 Selective determination of caffeine in foods with 3D-graphene based ultrasound-assisted magnetic solid phase extraction *Food Chem.* **262** 206–14

[47] Bang G S, So H-M, Lee M J and Ahn C W 2012 Preparation of graphene with few defects using expanded graphite and rose bengal *J. Mater. Chem.* **22** 4806

[48] Xiang D, Bo X, Gao X, Du C, Li P, Zhu L and Chen W 2019 Bimetal- and nitrogen-codoped spherical porous carbon with efficient catalytic performance towards oxygen reduction reaction in alkaline media *J. Colloid Interface Sci.* **534** 655–64

[49] Huang K-J, Wu Z-W, Wu Y-Y and Liu Y-M 2012 Electrochemical immunoassay of carcinoembryonic antigen based on TiO_2–graphene/thionine/gold nanoparticles composite *Can. J. Chem.* **90** 608–15

[50] Wang L, Zheng J, Yang S, Wu C, Liu C, Xiao Y, Li Y, Qing Z and Yang R 2015 Two-photon sensing and imaging of endogenous biological cyanide in plant tissues using graphene quantum dot/gold nanoparticle conjugate *ACS Appl. Mater. Interfaces* **7** 19509–15

[51] Wang Y, Zhang S, Du D, Shao Y, Li Z, Wang J, Engelhard M H, Li J and Lin Y 2011 Self assembly of acetylcholinesterase on a gold nanoparticles–graphene

nanosheet hybrid for organophosphate pesticide detection using polyelectrolyte as a linker *J. Mater. Chem.* **21** 5319

[52] Hou T L J L, Li G F, Zou Z X, Li L P and Wu M YS, Development of an immunomagnetic bead-based time-resolved fluorescence immunoassay for rapid determination of levels of carcinoembryonic antigen in human serum *Anal. Chim. Acta* **734** 93–8

[53] Yamauchi Y, Tonegawa A, Komatsu M, Wang H, Wang L, Nemoto Y, Suzuki N and Kuroda K 2012 Electrochemical synthesis of mesoporous Pt-Au binary alloys with tunable compositions for enhancement of electrochemical performance *J. Am. Chem. Soc.* **134** 5100–9

[54] Huang J, Tian J, Zhao Y and Zhao S 2015 Ag/Au nanoparticles coated graphene electrochemical sensor for ultrasensitive analysis of carcinoembryonic antigen in clinical immunoassay *Sensors Actuators* B **206** 570–6

[55] Shu H, Wen W, Xiong H, Zhang X and Wang S 2013 Novel electrochemical aptamer biosensor based on gold nanoparticles signal amplification for the detection of carcinoembryonic antigen *Electrochem. Commun.* **37** 15–9